



**SETCOR**  
Conferences & Exhibitions

**The Plasma Tech and SICT International Joint Conference**

**Plasma Tech 2021**  
**SICT 2021**

**Conference Proceedings**

**PLASMA PROCESSING  
AND TECHNOLOGY  
INTERNATIONAL CONFERENCE**

**07 - 09 APRIL, 2021  
PARIS - FRANCE**

**PLASMA  
TECH 2021**

**SURFACES, INTERFACES  
AND COATINGS TECHNOLOGIES  
INTERNATIONAL CONFERENCE**

**SICT  
2021**

**07 - 09 APRIL, 2021 | PARIS - FRANCE**

DOI: <https://doi.org/10.26799/cp-plasmatech-sict-2021>

## **Optical emission spectroscopy and actinometry in SF<sub>6</sub>/Ar RF discharges for PCE**

**Artem A. Osipov<sup>1,2,3</sup>, Vladimir I. Berezenko<sup>2</sup>, Armenak A. Osipov<sup>3</sup>, Anastasiya B. Shpeshilova<sup>2</sup>, Ekaterina V. Endiiarova<sup>2</sup>, Alina E. Gagaeva<sup>2</sup>, Sergey E. Alexandrov<sup>2</sup>**

<sup>1</sup>Alferov Federal State Budgetary Institution of Higher Education and Science Saint Petersburg National Research Academic University of the Russian Academy of Sciences, Saint Petersburg, Russian Federation, [tema.osipov@mail.ru](mailto:tema.osipov@mail.ru)

<sup>2</sup>Higher School of Physics and Materials Engineering, Peter the Great St. Petersburg Polytechnic University, Saint Petersburg, Russian Federation

[berezenko.vi@mail.ru](mailto:berezenko.vi@mail.ru), [speshilova\\_ab@spbstu.ru](mailto:speshilova_ab@spbstu.ru), [alina.gagaeva@mail.ru](mailto:alina.gagaeva@mail.ru), [endiyarovae@gmail.com](mailto:endiyarovae@gmail.com), [sevgalexandrov@gmail.com](mailto:sevgalexandrov@gmail.com)

<sup>3</sup>Southern-Urals Federal Research Center of Mineralogy and Geoecology, Institute of Mineralogy, Ural Branch, Russian Academy of Sciences, Miass, Russian Federation, [armik@mineralogy.ru](mailto:armik@mineralogy.ru)

### **Abstract**

This study investigates the optical-emission spectra (OES) of inductively-coupled plasma (ICP) discharges of SF<sub>6</sub>/ Ar gas mixtures. The impact of the key process parameters of the plasma-chemical etching (PCE) on fluorine radicals concentration has been studied using the optical emission actinometry. It was found that increase of SF<sub>6</sub> flow rate within a range between 1,5 sccm and 11,7 sccm leads to an increase in atomic fluorine concentration by 6 times, while reduction of the process pressure during the PCE from 1,65 Pa to 0,65 Pa provides an increase in atomic fluorine concentration more than 1,5 times, and an increase in the RF power absorbed in the plasma from 500 to 700 W is accompanied by an increase in the concentration of fluorine atoms by 1.27 times. The temperature of the substrate holder and the substrate bias voltage have no effect on the concentration of atomic fluorine in the plasma.

**Keywords:** plasma etching, ICP, OES, plasma diagnostics, optical emission actinometry

### **1. Introduction**

Currently, the technology of dry PCE is actively used for isotropic and anisotropic etching of wide range of semiconductor materials along with plasma cleaning of substrates with minimal surface damage caused by ion bombardment. PCE processes are based on chemical reactions involving highly reactive plasma species and processes of physical interaction between high-energy ions and the surface of the processed material. The use of PCE processes in microelectronics made it possible to successfully address most of the technological challenges in the production of modern nanostructures. [1], [2].

However, PCE processes are characterized by a complex mechanism, which make it important not only to know the nature of the influence of the process parameters on the etching rate, anisotropy, selectivity, and surface roughness, but also to understand how they affect to the properties of the plasma itself.

At present, a variety of instrumental methods of plasma diagnostics are used, among which optical spectroscopy method stands out because of its capability of determination of the electron density, electron temperature and electron energy distribution function (EEDF), as well as to obtain information about processes of radical formation in the plasma without disturbing the system under study.[3]–[7].

## 2. Experimental

The experiments were carried out with specially made original equipment that allows implementing the plasma chemical etching processes of various electronic materials in a high-density inductively-coupled plasma (Figure 1 As can be seen from Figure 1c, the process reactor of the PCE tool consists of two chambers: a discharge chamber and a reaction chamber. The discharge in the discharge chamber was created by applying high-frequency (HF) power to the inductor of a special geometry from the RF generator ( $f = 6.78$  MHz,  $W_{\max} = 1000$  W) through a resonant matching device. To create the bias potential, an RF voltage of 13.56 MHz frequency was applied to the substrate holder (electrode) from a separate RF generator. The substrate holder was equipped with both a water-cooled unit (flow-through cooling system) and integrated resistive heating element (figure 1-a) [8], [9].

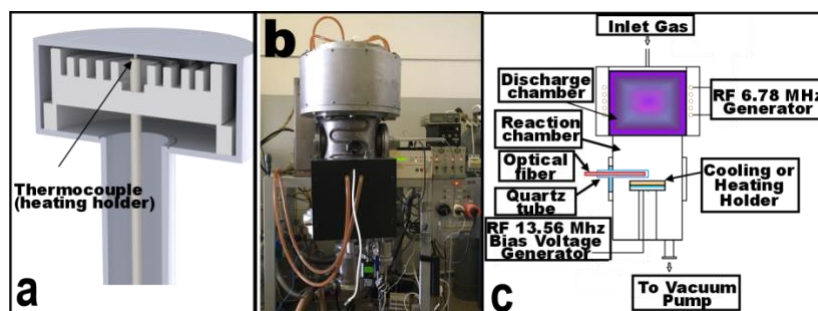


**Figure 1.** a) 3D CAD drawing of the substrate holder with a built-in heater, b) general view of the PCE system, c) schematic drawing of the processing and plasma chambers

Experiments to investigate the effect of RF power ( $W_{RF}$ ), bias voltage ( $U_{bias}$ ), chamber pressure ( $P$ ), and  $SF_6$  flow rate ( $Q_{SF_6}$ ) on the concentration of fluorine atoms in plasma were carried out using a water-cooling unit of the substrate holder.

The emission spectra of the gas discharge in the chamber were recorded using an OceanOptics HR 4000 spectrometer in the wavelength range of 200 – 1120 nm with a resolution of  $\sim 0.02$  nm. The spectra were recorded directly in the reactor at a height of 5 mm from the center of the substrate holder (Figure. 1 c).

## 3. Results and discussion

Figure 2 represents the emission spectra of plasma generated in pure Ar and  $SF_6$  environment using discharges maintained under the conditions presented in Table 1. To analyze the effect of plasma generation conditions on its spectral characteristics, three lines (750.7, 811.5, and 842.2 nm) in the argon plasma spectrum and four lines (685.7, 703.8, 720.3, and 775.5) in the  $SF_6$  plasma spectrum were selected [10]–[13].

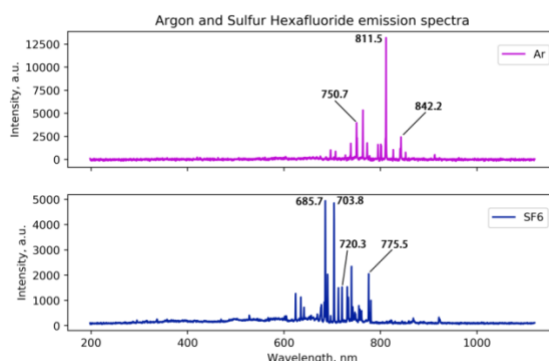


**Figure 2.** Optical emission spectra of argon and  $SF_6$  plasmas [13].

The concentration of fluorine atoms for SF<sub>6</sub> plasmas was estimated for the discharges maintained under the conditions presented in Table 2. The values of HF power, the bias voltage, and the temperature of the substrate holder were fixed and equal to 700 W, -50 V, and 15 °C, respectively. The gas pressure was set in such a way that it coincided with the partial pressure of the SF<sub>6</sub>/Ar gas mixtures (listed above) of different ratios prior to the moment of plasma generation.

Table 2: Parameters of Optical Actinometry Experiments

Q <sub>SF<sub>6</sub></sub> , sccm	1.5	4.7	7.0	7.8	9.4	11.7
P, Pa	0.15	0.30	0.45	0.50	0.60	0.65

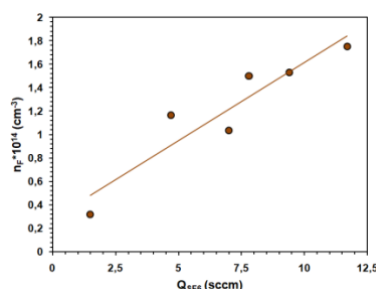


Figure 3. Dependence of the concentration of fluorine atoms on the SF<sub>6</sub> flow rate

As expected, an increase of sulfur hexafluoride flow rate leads to the strongest increase in the concentration of fluorine atoms (Fig. 4) due to a respective increase of the partial pressure of SF<sub>6</sub>. The maximum concentration of fluorine atoms in SF<sub>6</sub> plasma was observed at a maximum flow rate of 11.7 sccm SF<sub>6</sub>. Due to the fact that in order to achieve high rates of the PCE process maximum concentrations of the active component are needed, and further studies aimed at determining the nature of the influence of the remaining technological parameters on the concentration of fluorine atoms in the plasma were carried out at this SF<sub>6</sub> flow rate.

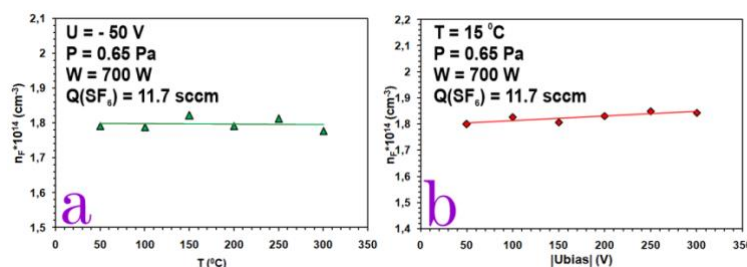
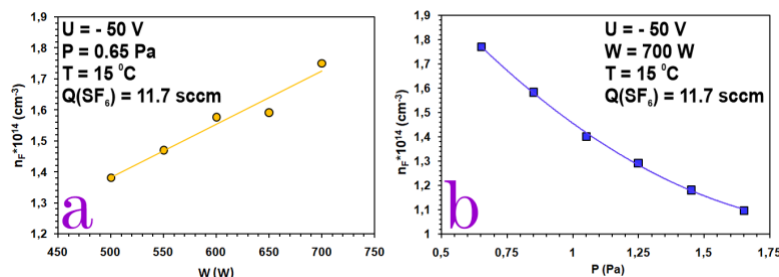


Fig. 4. a - a – n<sub>F</sub> vs holder temperature, b – n<sub>F</sub> vs bias voltage

The actinometry data presented in Fig. 4 (a, b) demonstrated slight influence of holder temperature and bias voltage on the concentration of atomic fluorine in the reaction medium.

However, as shown by the results of the study of the nature of the influence of HF power and pressure on the concentration of fluorine atoms in SF<sub>6</sub> plasma at a fixed gas flow rate (11.7 sccm), it was shown that the technological parameters that determine the concentration and average electron energy play a critical role in the concentration of chemically active fluorine. It can be seen from the data presented in Fig. 5 (a, b) that an increase in the absorbed power leads to a significant increase in the concentration of fluorine atoms, and an increase in pressure is accompanied by a decrease in the concentration of fluorine atoms in the selected range of technological parameters.



**Figure 5.** a-  $n_F$  vs. applied HF power,  $W$ ; b -  $n_F$  vs. process pressure

The amount of power consumed by the discharge determines concentration and mean energy of electrons in plasma, hence significantly affects the rate of chemically active particles formation in plasma. With an increase in the absorbed power both of these characteristics rise, which leads to an increase in the frequency of inelastic collisions of electrons with atoms or molecules of the gas mixture and a parallel increase in the concentration of chemically active particles and ions in the plasma, in this case – fluorine atoms (fig. 5 a) [14].

As can be seen from the figure 5 b, a decrease in pressure leads to an increase in the concentration of fluorine atoms in the plasma. The decrease in pressure should lead to an increase in the free path of the electrons and therefore to an increase in their energy, which as in the case of HF power should be accompanied by an increase in the concentration of fluorine in the selected range of technological parameters.[15].

#### 4. Conclusion

The outcome of the performed studies are the results describing the nature of the influence of the main technological parameters of the sulfur hexafluoride based plasma-chemical etching process on the concentration of atomic fluorine in the reaction medium which is the main highly reactive component responsible for etching many electronic materials. It is shown that an increase in the  $\text{SF}_6$  flow rate within the range of 1.5-11.7 sccm caused an increase in the concentration of atomic fluorine by 6 times, while a decrease in the process pressure of the PCE process from 1.65 Pa to 0.65 Pa leads to an increase in the concentration of fluorine atoms in the plasma by more than 1.5 times, and an increase in the RF power absorbed in the plasma from 500 to 700 W is followed by an increase in the concentration of fluorine atoms by 1.27 times. The temperature of the substrate holder and the bias voltage have no effect on the concentration of atomic fluorine in the plasma.

#### Acknowledgements

The reported study was funded by RFBR, project number 19-32-60023

#### References

- [1] K. Nojiri, *Dry etching technology for semiconductors*. 2015.
- [2] V. M. Donnelly and A. Kornblit, “Plasma etching: Yesterday, today, and tomorrow,” *J. Vac. Sci. Technol. A Vacuum, Surfaces, Film.*, vol. 31, no. 5, p. 50825, 2013.
- [3] A. D. Srivastava, M. H. Gordon, and D. G. Bhat, “Optical emission spectroscopy in an inverted cylindrical magnetron plasma,” *Surf. Coatings Technol.*, vol. 200, no. 5–6, pp. 1346–1350, 2005.
- [4] Y. Miyoshi, M. Miyauchi, A. Oguni, and T. Makabe, “Optical diagnostics for plasma-surface interaction in  $\text{CF}_4/\text{Ar}$  radio-frequency inductively coupled plasma during Si and Si O 2 etching,” *J. Vac. Sci. Technol. A Vacuum, Surfaces, Film.*, vol. 24, no. 5, pp. 1718–1724, 2006.
- [5] X.-M. Zhu and Y.-K. Pu, “Using OES to determine electron temperature and density in low-pressure nitrogen and argon plasmas,” *Plasma Sources Sci. Technol.*, vol. 17, no. 2, p. 24002, 2008.
- [6] M. Sabsabi, S. Vacquié, D. V Gravelle, and M. I. Boulous, “Emission spectroscopic study of a

- low pressure supersonic Ar-H<sub>2</sub> DC plasma jet,” *J. Phys. D. Appl. Phys.*, vol. 25, no. 3, p. 425, 1992.
- [7] A. A. Osipov, A. A. Osipov, V. I. Berezenko, and S. E. Alexandrov, “Using OES to measurement of electron temperature of SF<sub>6</sub>/Ar gas mixture of ICP discharges,” in *Journal of Physics: Conference Series*, 2020, vol. 1679, no. 2, p. 22006.
- [8] A. A. Osipov, G. A. Iankevich, and S. E. Alexandrov, “Monocrystalline quartz ICP etching: Road to high-temperature dry etching,” *Plasma Chem. Plasma Process.*, vol. 40, no. 1, pp. 423–431, 2020.
- [9] A. A. Osipov *et al.*, “High-temperature etching of SiC in SF<sub>6</sub>/O<sub>2</sub> inductively coupled plasma,” *Sci. Rep.*, vol. 10, no. 1, pp. 1–10, 2020.
- [10] J. Ma, M. N. R. Ashfold, and Y. A. Mankelevich, “Validating optical emission spectroscopy as a diagnostic of microwave activated CH<sub>4</sub>/Ar/H<sub>2</sub> plasmas used for diamond chemical vapor deposition,” *J. Appl. Phys.*, vol. 105, no. 4, p. 43302, 2009.
- [11] A. Sarani, A. Y. Nikiforov, and C. Leys, “Atmospheric pressure plasma jet in Ar and Ar/H<sub>2</sub>/O mixtures: Optical emission spectroscopy and temperature measurements,” *Phys. Plasmas*, vol. 17, no. 6, p. 63504, 2010.
- [12] S. P. Koirala, M. H. Gordon, L. Cai, S. L. Burkett, and L. W. Schaper, “Optical Emission Spectroscopy in a Reactive Ion Etching System,” in *2007 IEEE Region 5 Technical Conference*, 2007, pp. 189–193.
- [13] A. A. Osipov, A. A. Osipov, V. I. Berezenko, and S. E. Alexandrov, “OES diagnostic of SF<sub>6</sub>/Ar gas mixture of ICP discharges for LiNbO<sub>3</sub> etching,” in *IOP Conference Series: Materials Science and Engineering*, 2020, vol. 919, no. 2, p. 22018.
- [14] A. You, M. A. Y. Be, and I. In, “Observations of argon emission lines used for fluorine atom actinometry in low power rf discharges,” vol. 1042, no. June 1998, pp. 10–13, 2002.
- [15] T. H. Chung, Y. W. Lee, H. M. Joh, and M. A. Song, “Pressure dependence of dissociation fraction and optical emission characteristics in low-pressure inductively coupled N<sub>2</sub>-Ar plasmas,” *AIP Adv.*, vol. 1, no. 3, p. 32136, 2011.

# Mean Absorption Coefficients of air-copper thermal plasmas at atmospheric pressure

Raveloharinjaka E.<sup>1,2</sup>, Cressault Y.<sup>1</sup>, Rakotomalala M.<sup>2</sup>, Randrianandraina H.Z.<sup>2</sup>

<sup>1</sup> Université de Toulouse, UPS, INPT, LAPLACE (Laboratoire PLasma et Conversion d'Energie), 118 Route de Narbonne, F-31062 Toulouse Cedex 9, France, [elise.raveloharinjaka@laplace.univ-tlse.fr](mailto:elise.raveloharinjaka@laplace.univ-tlse.fr)  
[yann.cressault@laplace.univ-tlse.fr](mailto:yann.cressault@laplace.univ-tlse.fr)

<sup>2</sup> University of Antananarivo, Institut pour la Maitrise de l'Energie, BP566, Antananarivo 101, Madagascar

## Abstract

This work focuses on the radiative transfer of in air-copper thermal plasmas using its Mean Absorption Coefficients (MACs). The spectral absorption coefficients are obtained by the line-by-line method from 300K to 30000K, 30nm to 4500nm at atmospheric pressure and by assuming the plasma in Local Thermodynamic Equilibrium. These wavelengths are splitted into several spectral intervals and the average of the absorption coefficients are calculated in each of them using different means. We compare these means, the corresponding Radiative Flux (RF) and Divergences of the Radiative Flux (DRF) with the exact resolution of the Radiative Transfer Equation to conclude which mean is adapted or not to air-copper thermal plasma according to the temperature, wavelength, and mixture ranges.

**Keywords:** air copper plasma, thermal plasma, radiative transfer, radiative proprieties, metallic vapour, mean absorption coefficient, radiative flux, divergence of the radiative flux.

## 1. Introduction

Air-copper thermal plasmas can be found on electrical installations composed of copper especially in Madagascar where they are subject to aging and to strong variations of the climate. The radiation emitted by the electric arc of air with metallic vapours of copper can damage surrounding materials like cables. Studying this radiation by resolving its Radiative Transfer Equation (RTE) may help to protect these surrounding materials. In this paper, we have calculated the Mean Absorption Coefficient to describe more easily the radiative transfer of the plasma. The first step of this method is to divide the spectrum into several intervals. We present two examples of plasma: pure air and [50%] air – [50%] cu in mass proportions, to show the influence of metallic vapours on the choice of these intervals. Next, we calculate the average of the absorption coefficient [1] inside of each interval using five means: the classic mean, the Planck mean, the Planck modified mean, the Rosseland mean and the hybrid Planck-Rosseland mean. We compare their value in each interval to show their difference. At the end, we calculate the Radiative Flux (RF) and the Divergence of the Radiative Flux (DRF) for some plasmas, according a given temperature profile and these means and we compare these results with those obtained by resolving the RTE in the case of a 1D model.

## 2. The spectral intervals

For the MAC method, the spectral intervals should be well defined to well describe the spectrum and their number should not be so high to avoid very long computation times. In the literature, the number of spectral intervals does not exceed 10 and the spectra limits are defined according the abrupt changes of the spectral absorption coefficient. For a pure air plasma, we divide all the radiative spectra into six wavelengths intervals (table 1). The limits correspond to the ionization of N (14.534eV, 85.3nm) and to different excitations [2]. For the [50%] air-[50%] cu plasma mixture, the spectrum is divided into 7 bands (table 2), one spectral interval being added to take into account the ionization of the copper (7.726eV, 160.4nm).

Table 1: The spectral intervals in wavelength  $\lambda$  (frequency  $\nu$ ) for a pure air plasma

band	1	2	3	4	5	6
$\lambda$ (nm)	30-85.3	85.3-101.9	101.9-113	113-194.6	194.6-856.5	856.5-4500
$\nu$ ( $10^{15}$ Hz)	10-3.52	3.52-2.94	2.94-2.65	2.65-1.54	1.54-0.35	0.35-0.06

Table 2: The spectral intervals in wavelength  $\lambda$  (frequency  $\nu$ ) for a [50%] Air-[50%] Cu plasma

band	1	2	3	4	5	6	7
$\lambda$ (nm)	30-85.3	85.3-101.9	101.9-113	113-160.4	160.4-194.6	194.6-856.5	856.5-4500
$\nu$ ( $10^{15}$ Hz)	10-3.52	3.52-2.94	2.94-2.65	2.65-1.87	1.87-1.54	1.54-0.35	0.35-0.06

### 3. The means

Five means are found in the literature to calculate the MAC for each spectral interval: the classic mean, the Planck mean, the Planck modified (mod) mean, the Rosseland mean and the hybrid Planck-Rosseland (P-R) mean [3]. Their expressions are presented below (Table 3).

Table 3: The expressions of means used in calculation of the MACs in a band  $[\lambda_i, \lambda_j]$

The classic mean: (1) $\bar{K}'_C = \frac{\int_{\lambda_i}^{\lambda_j} K'(\lambda, T) d\lambda}{\int_{\lambda_i}^{\lambda_j} d\lambda}$	The Planck mean: (2) $\bar{K}'_P = \frac{\int_{\lambda_i}^{\lambda_j} K'(\lambda, T) \cdot L_{\lambda}^0(T) d\lambda}{\int_{\lambda_i}^{\lambda_j} L_{\lambda}^0(T) d\lambda}$
The Planck modified mean: (3) $\bar{K}'_{PM} = \frac{\int_{\lambda_i}^{\lambda_j} K'(\lambda, T) \cdot L_{\lambda}^0(T) \exp(-K'(\lambda, T) \cdot R) d\lambda}{\int_{\lambda_i}^{\lambda_j} L_{\lambda}^0(T) d\lambda}$ R is the radius of the plasma	The Rosseland mean: (4) $\bar{K}'_R = \frac{\int_{\lambda_i}^{\lambda_j} \frac{dL_{\lambda}^0(T)}{dT} d\lambda}{\int_{\lambda_i}^{\lambda_j} \frac{dL_{\lambda}^0(T)}{dT} \cdot \frac{1}{K'(\lambda, T)} d\lambda}$
The hybrid Planck-Rosseland mean: (5) $\bar{K}'_{HPR} = (1 - \gamma) \cdot \bar{K}'_P + \gamma \cdot \bar{K}'_R \text{ where } \gamma = \frac{(\bar{K}'_P - \bar{K}'_R)}{\bar{K}'_P}$	

$K'(\lambda, T)$  is the absorption coefficient in each wavelength  $\lambda$  inside the interval  $[\lambda_i, \lambda_j]$

$\frac{dL_{\lambda}^0(T)}{dT}$  is the derivative of the Planck function  $L_{\lambda}^0(T)$  with respect to the temperature T

The Planck modified mean depends on the plasma radius R. In this study, we choose R=1mm and R=5mm for this mean.

### 4. The MAC in each interval

We have established a database of the MACs in each interval for the temperature range between 300K and 30000K of different proportions of air and copper metallic vapours. In this work, we present only two examples to highlight the differences observed between the means: pure air and [50%] air – [50%] cu plasmas at temperature T=5000K and T=10000K under the atmospheric pressure (P=1atm).

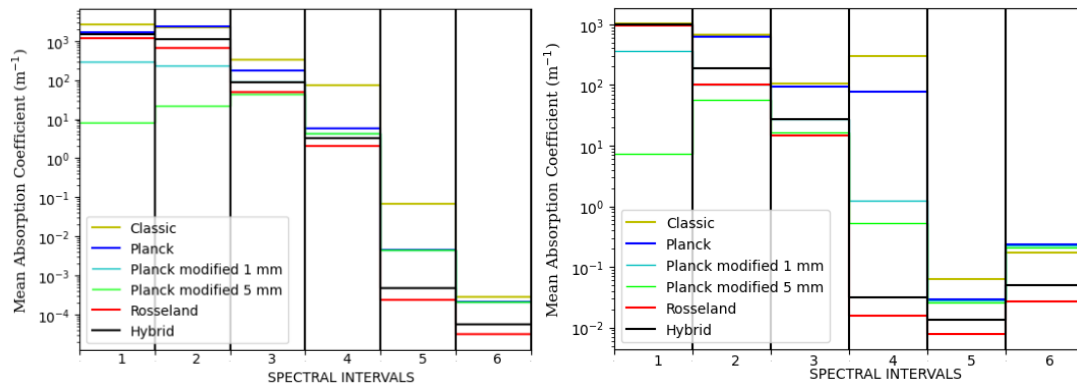


**Figure 1 & 2:** MACs for air pure plasma in the 6 intervals, for  $P=1\text{atm}$ ,  $T=5000\text{K}$  (left) and  $T=10000\text{K}$  (right)

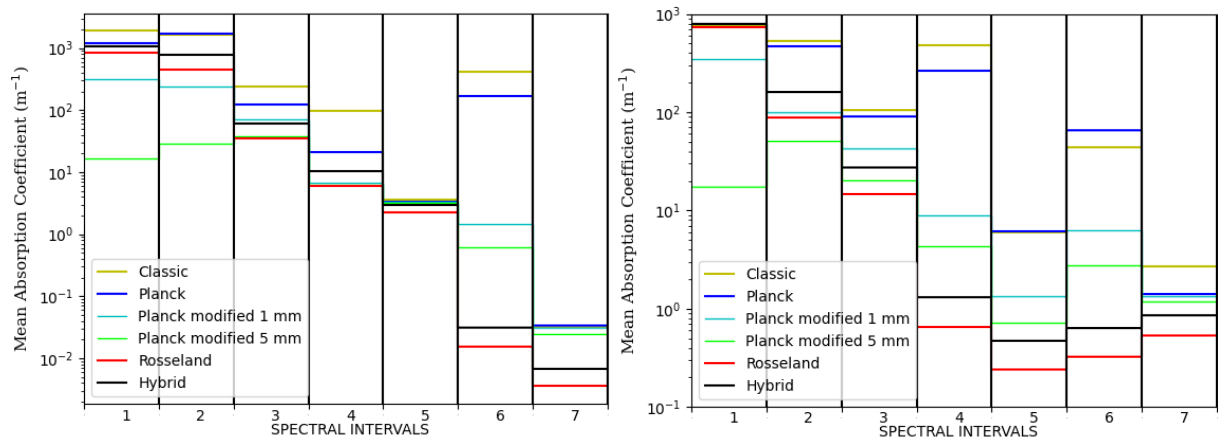


**Figure 3 & 4:** MACs for [50%]-[50%] air-cu plasma in the 7 spectral intervals, for  $P=1\text{atm}$ ,  $T=5000\text{K}$  (left) and  $T=10000\text{K}$  (right)

From the figures (fig1 to 4), we can observe that the values from the classic and Planck means are higher than the others and that the Rosseland mean gives values lower than the others. The hybrid Planck Rosseland being a combination of the Planck and the Rosseland means, its value is always between theirs. With the Planck modified mean ( $R=1\text{mm}$  and  $R=5\text{mm}$ ), MACs at  $5000\text{K}$  are greater than  $10000\text{K}$  due to a stronger by absorption by the molecules (higher population number densities at  $5000\text{K}$ ). The difference between pure air and [50%] air-[50%] cu plasmas is especially visible in spectral (intervals 5 and 6) where the atomic lines of copper are more numerous due to a low ionization potential of the copper ( $7.726\text{eV}$ ).

## 5. The Radiative Flux and Divergence of the Radiative Flux of each MAC

In this part, the RF and the DFR have been calculated from the MACs and compared with an exact resolution of the RTE in a 1D case. We assume an axisymmetric temperature profile divided in 100 meshes (centre to edge), decreasing from a maximal temperature of  $20000\text{K}$  on its centre (at  $X=0\text{mm}$ ) to  $300\text{K}$  on its edge (at  $X=20\text{mm}$ )

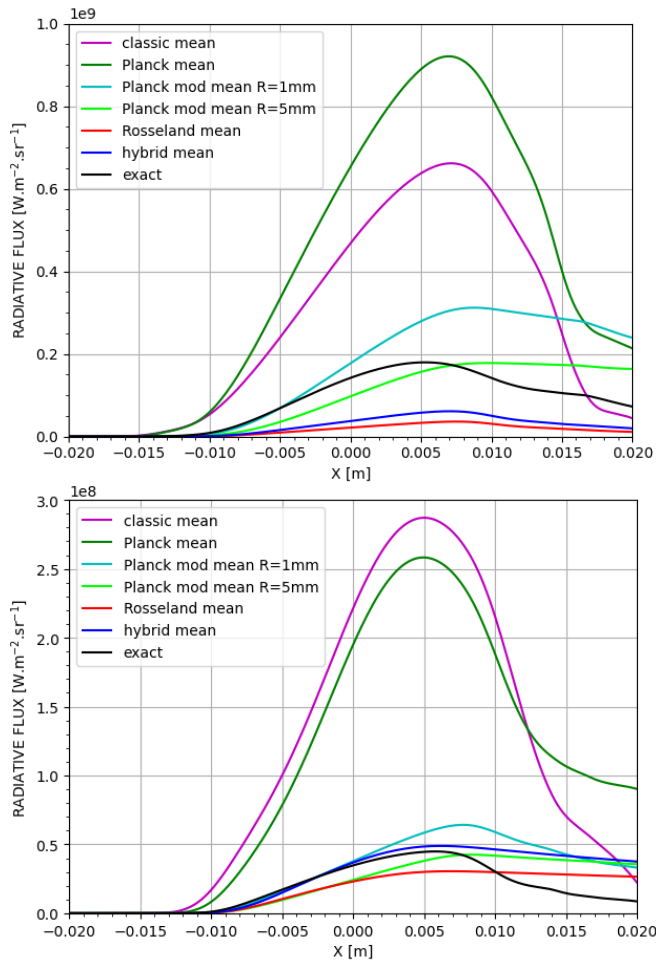


**Figure 5 & 6:** Comparison of the RF obtained from MACs and exact resolution of the RTE, 1atm, for pure air (left) and [50%] air-[50%] cu plasma (right)

Firstly, we can observe that mixture with copper vapours has greater RF than the pure air because of the presence of a strong emission from the copper lines [4]. Then, the results highlight that RF deduced from classic and Planck means are extremely greater compared to the values obtained from the exact resolution of the RTE. In other hand, the Rosseland mean underestimates the RF in the case [50%] air-[50%] cu mixture (fig.6). The value from hybrid P-R overlaps the first half of the exact value in the fig.5 but underestimates it in the fig.6. This mean depends extremely on the Rosseland mean. For the Planck modified mean, the first half of the exact value overlaps also its result with R=1mm in the fig.5 but has the same RF as the result with R=5mm in the fig.6.

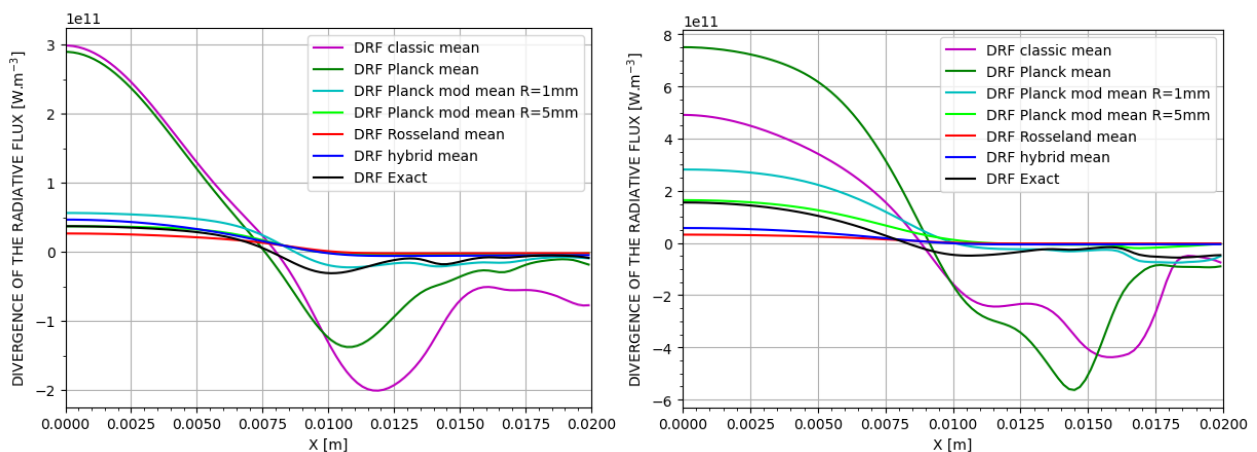


**Figure 7 & 8:** Comparison of the DRF of MACs with the exact resolution of the RTE at P=1atm, respectively for a [100%] Air plasma and a [50%] Air-[50%] Cu plasma mixture under P=1atm

For pure air plasma (fig.7), three drops can be seen in the variation of the DRF. The first (at 0.01m) corresponds to the absorption of the radiation for the ionization of the N into N<sup>+</sup> near 13000K. The second (at 0.014m) and the third (at 0.016m) drops are the absorption to dissociate molecules to produce azote atom (near 7000K) and oxygen atom (near 3000K). For the [50%] Air-[50%] Cu plasma mixture (fig.8), a diminution of the DRF is noticed near the edge of the plasma because of the absorption of the radiation to dissociate molecules and to produce copper atom near 3000K.

## 6. Conclusion

The spectrum is splitted into six spectral intervals for the pure air plasma and into seven spectral intervals for the [50%] air-[50%] cu plasma. In these intervals, the classic and Planck mean of the absorption coefficient are higher than the others, the Rosseland mean has generally the lower value and the hybrid is always between of them. With the Planck modified mean, the more the radius of the plasma increases, the lower the value is. The comparison of their RF and DRF with those of the exact resolution of the RTE highlight that the classic and Planck means are not adapted to calculate the MACs of the air-copper thermal plasma. Their values are extremely higher. The Planck modified can approach the exact results but its plasma radius needs to be well defined. The hybrid mean can be also approaching the exact results but it depends too much on the Rosseland mean. When air is mixed with copper, the presence of the copper atomic lines and their strong emission increases strongly the emission in the plasma.

## Reference

1. A. Gleizes et Y. Cressault, « Effect of Metal Vapours on the Radiation Properties of Thermal Plasmas », *Plasma Chem. Plasma Process.*, vol. 37, n° 3, p. 581-600, 2017.
2. R. Hannachi, Y. Cressault, D. Salem, P. Teulet, L. Béji, et Z. Ben Lakhdar, « Mean absorption coefficient of H<sub>2</sub>O-air-MgCl<sub>2</sub>/ CaCl<sub>2</sub>/NaCl thermal plasmas », *J. Phys. D. Appl. Phys.*, vol. 45, n° 48, 2012.
3. S. Kozu, et al. « Radiative transfer calculation of CO<sub>2</sub> thermal plasma using a hybrid Planck-Rosseland mean absorption coefficient », *Proc. 22nd Int. Conf. Gas Discharges Their Appl.*, p. 127-130, 2018.
4. R. Hannachi, Y. Cressault, P. Teulet, A. Gleizes, J. P. Gonnet, et J. Y. Battandier, « Influence of metallic vapours on the properties of air thermal plasmas », *Plasma Sources Sci. Technol.*, vol. 17, n° 3, 2008

# Fabrication of Tungsten high aspect ratio micro-tools by electrochemical etching, by controlling the immersed length and the etching charge

Asmae Taфраouti, Pascal Kleimann, Yasmina Layouni

Université de Lyon, Institut des Nanotechnologies de Lyon, UMR 5270 CNRS INSA ECL UCB CPE  
Bât L.Brillouin, F69622 Villeurbanne, France; [asmae.taфраouti@univ-lyon1.fr](mailto:asmae.taфраouti@univ-lyon1.fr), [yasmina.layouni@cpe.fr](mailto:yasmina.layouni@cpe.fr),  
[pascal.kleimann@univ-lyon1.fr](mailto:pascal.kleimann@univ-lyon1.fr)

## Abstract

This paper aims to present the fabrication of high aspect ratio cylindrical Tungsten micro-tools using electrochemical etching. The etching protocol has been optimized by controlling the immersed length and the etching charge which made it possible the automated fabrication of micro-tools with  $88\mu\text{m} \pm 1\mu\text{m}$  average diameter over 3,5mm length starting from  $250\mu\text{m}$  diameter Tungsten wires.

**Keywords:** Tungsten electrochemical etching, inhomogeneous etching, "drop-off" effect, and meniscus effect

## 1. Introduction

Tungsten micro-tools are extensively used in Electrical Discharge Machining EDM [1], Atomic Force Microscope AFM [2], Scanning Tunnelling Microscope STM [3], and medical applications [4]. Electrochemical etching is a low-cost, efficient and reproducible technique [5]. In this work, we have optimized this technique to fabricate high aspect ratio ( $\approx 100$ ) cylindrical micro-tools dedicated to micro-EDM machining. In this, we studied the influence of different parameters: (1) Electrical parameters such as the level and the shape of the applied voltage. (2) Geometrical parameters, as the distance between electrodes and the size of the etching cell. (3) Physico-chemical parameters such as the electrolyte concentration (NaOH in our case) and the temperature. Several teams have been interested in Tungsten electrochemical etching. Hobara's team [6] has shown that dynamic etching (vertical displacement of the micro-tool) produces conical micro-tools while static etching can lead to the fabrication of cylindrical micro-tools under specific conditions. A continuous etching polarization (of a few volts) leads to the formation of conical micro-tools with a low aspect ratio, whereas, a pulsed polarization produces micro-tools with a high aspect ratio.

The distance between the counter electrode and the micro-tool has also a great impact on the shape of the micro-tool. Positioning the counter electrode close to the micro-tool disturbs its etching due to the effect of hydrogen bubbles that propagate towards the air/solution interface, which makes the etching speed faster at the air-tool-solution interface (meniscus) and emphasizes the "drop-off" effect (Fig.1), leading to low aspect ratio micro-tools [1,7].

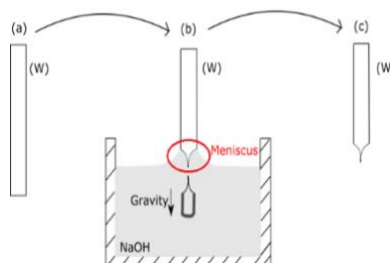


**Fig.1:** "Drop-off" effect, (a): initial micro-tool, (b): breakage of the micro-tool by "drop-off" effect, (c): final micro-tool

Based on these results from the literature, we have used a cell where the counter electrode is far from the micro-tool electrode. We also used a static etching (no agitation) and a low amplitude pulsed signal with ( $U=0,5V$ ). The etching of the micro-tool was performed at room temperature ( $25^{\circ}\text{C}$ ) using 4mol/l NaOH electrolyte.

## 2. Experimental

### 2.1. Experimental setup

The experimental setup (Figure.2), consists of an electrochemical cell with three electrodes, a working electrode (WE) represents the micro-tool made of pure Tungsten (99.95% [8]) with an initial diameter  $\Phi_0 = 250\mu\text{m}$ , a reference electrode (RE) made of Ag/AgCl, and a platinum counter electrode (CE). In order to avoid  $\text{H}_2$  hydrogen bubbles that disrupt the etching at the meniscus (air-tool-solution interface), the counter electrode and the working electrode are placed 8cm apart. The setup is PC-controlled and includes a source meter (Keithley 2401) that controls the applied voltage and the etching charge, and a Z-motorisation that controls the micro-tool diving depth.

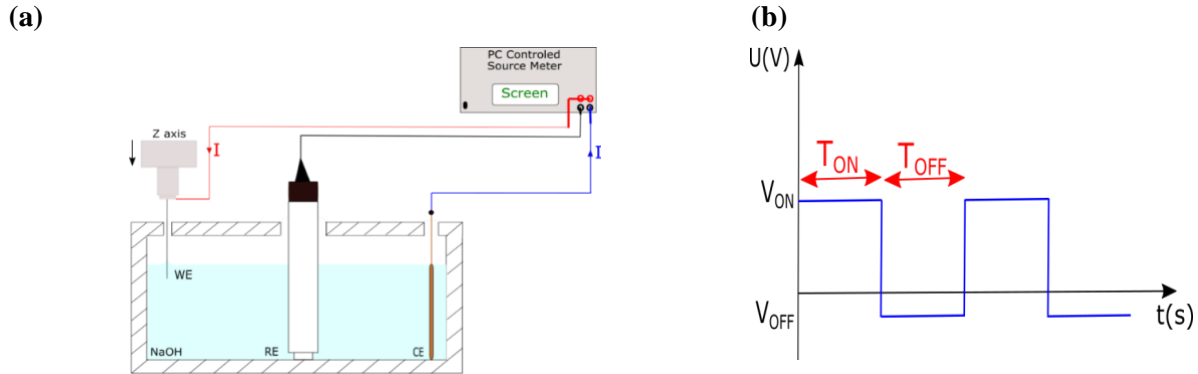


**Fig.2:** (a) Experimental setup, (b) Type of the applied signal during the electrochemical etching

During the anodic etching of the micro-tool, the global equation of the electrochemical reaction is [1,2]:



The average diameter is determined by the following equation [1]:

$$\Phi = \sqrt{\Phi_0^2 - \left( \frac{4 \cdot M \cdot Q}{\pi \cdot L \cdot \rho \cdot z \cdot F} \right)} \quad (2)$$

Where  $\Phi_0$  is the initial diameter of the micro-tool;  $M=185.85$  g/mol the Tungsten molar mass;  $Q$  the etching charge;  $L$  the length immersed in the solution;  $\rho=19300$  Kg/ $m^3$  the Tungsten volumic mass;  $z=6$  the valence of the electrochemical reaction in the case of Tungsten;  $F=96485$  C/mol the Faraday constant.

### 2.2. Protocols used during electrochemical etching

The first step consists in performing a  $I(V)$  curve (Fig. 3a). This step allows us to ensure that the Tungsten wire is well placed and to strip it before etching.

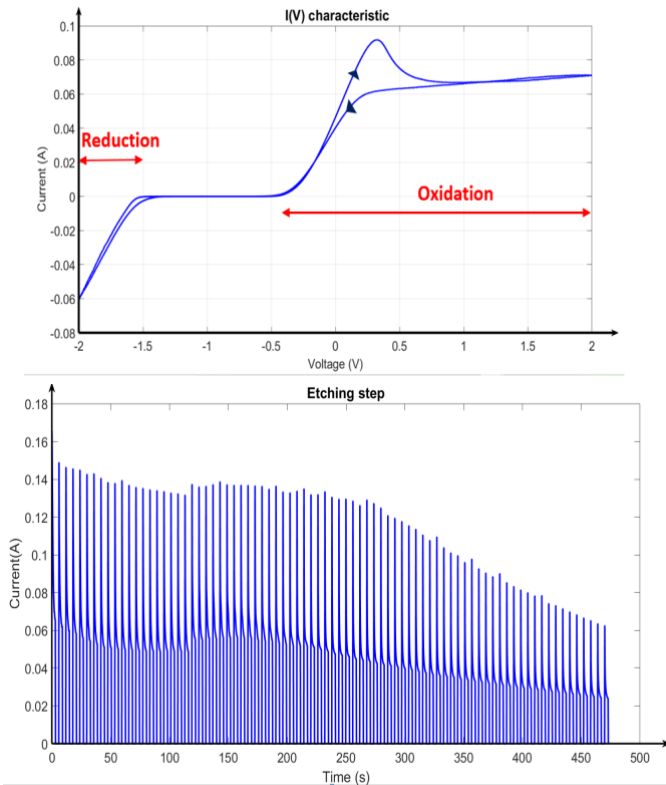


**Fig. 3:** (a) The I(V) characteristic, (b) Etching step

For the etching step (Figure. 3b), the applied voltage is pulsed ( $T_{ON} = T_{OFF} = 3s$ ,  $V_{ON} = 0,5V$ ,  $V_{OFF} = -0,8V$ ). The ON-state voltage has been fixed to 0,5V: a lower voltage indeed leads to an inhomogeneous etching and a higher one leads to the loss of the micro-tool by "drop-off" effect. The OFF-state applied voltage has been fixed to -0,8V, that corresponds to zero etching current condition. The number of cycles depends on the final desired diameter.

### 3. Results and discussion

#### 3.1. Study of the reproducibility of electrochemical etching

First, we studied the reproducibility of the process. The initial micro-tool diameter is  $\Phi_0 = 250\mu m$ , the immersed length is  $L = 5mm$  and the etching charge is  $Q = 13,2C$ . Fig.4 shows the micro-tool profiles after etching for three samples. We notice that the micro-tools do not have the same shape on the upper part. However, they have almost the same profile on the lower part over a length of 3,5mm. To validate this protocol, we repeated the same experiment more than ten times. The average diameter is  $88 \mu m \pm 1 \mu m$ .

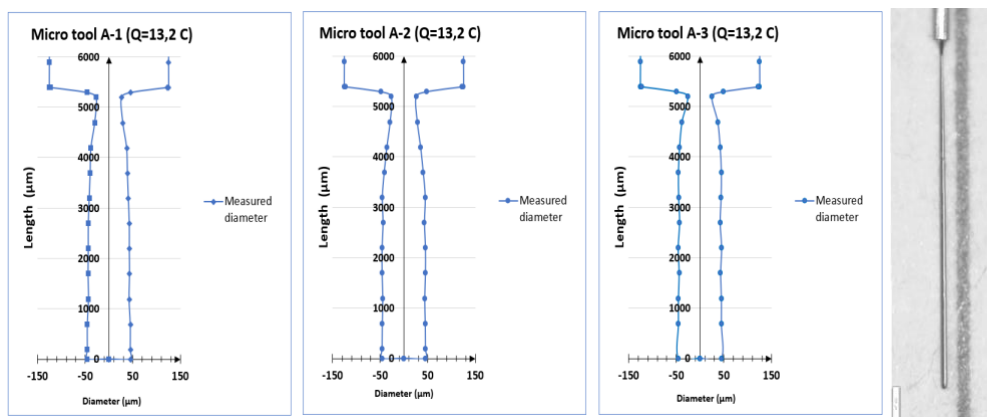


**Fig. 4:** Micro-tools profile obtained after etching for  $Q = 13,2C$  and a wire with an initial diameter  $\Phi_0 = 250\mu m$

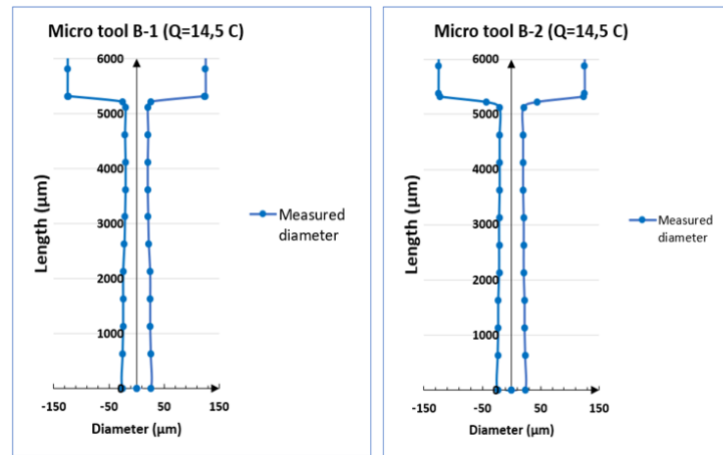


Fig. 5 : Micro-tools profile obtained after etching for  $Q=14,5C$  and a wire with an initial diameter  $\Phi_0 = 250\mu m$

In order to fabricate micro-tools with diameter lower than  $88 \mu m$ , the etching charge was increased to  $Q=14,5C$ . The average diameter is  $44 \mu m \pm 3\mu m$  over a length of  $3,5mm$  (Fig.5). However, the process is not reproducible and sometimes leads to the breakage of the micro-tool by "drop-off" effect.

This lack of reproducibility can be explained by the rapid decrease of the tool diameter at the end of the etching process, as shown in Fig.6. This can lead to a small diameter at the meniscus and thus result the tool breakage by "drop-off" effect.

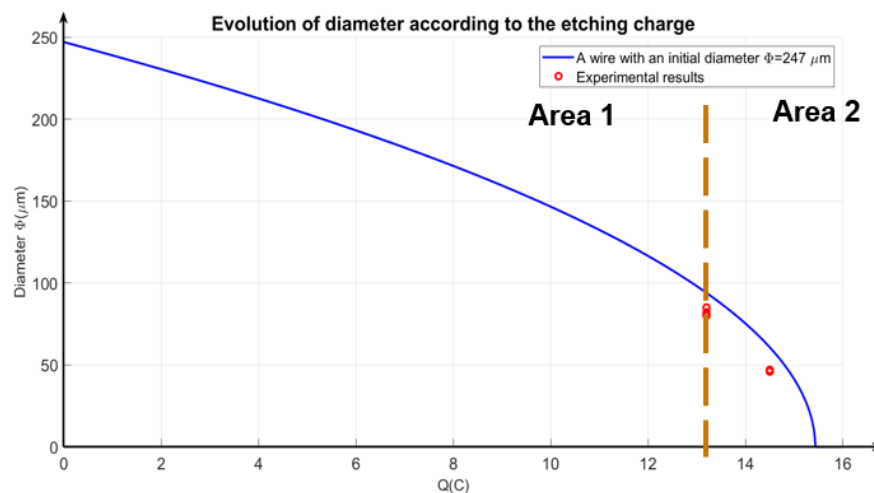


Fig.6: Evolution of the theoretical diameter according to the etching charge for a wire with an initial diameter  $\Phi_0 = 250\mu m$

#### 4. Conclusion

In this paper, we present a protocol to fabricate high aspect ratio micro-tools with diameter up to  $88\mu m$ . It is based, on the one hand, on the use of a cell where the working electrode is far from the counter electrode to limit the effect of hydrogen bubbles on the etching at the meniscus level. On the other hand, it is based on the combined control of the immersed length and the applied etching charge.

The formation of thinner tools requires an improvement of the etching protocol. First it is, of course, possible to use thinner Tungsten wires (i.e.  $\Phi_0=125\mu m$ ). Then, in order to solve the problem of the tool breakage, the immersed length can be controlled during the etching process. Finally, in order to have a better control of the tool diameter it is necessary to include an in-situ measurement.

## References

1. G. Girardin, « Développement d'un procédé d'usinage par micro-électroérosion », PhD thesis, UCBL, 2013
2. H. S. Lim et al, "A study on the machining of high-aspect ratio micro-structures using micro-EDM", *J. Mater. Process. Technol.*, vol. 140, no. 1–3, pp. 318–325, Sep. 2003.
3. B.-Y. Joo et al, "Micro-hole fabrication by mechanical punching process", *Journal of Materials Processing Technology*, vol. 170, no. 3, pp. 593–601, 2005.
4. J. E. Griffith et al, "Dimensional metrology with scanning probe microscopes", *Journal of Applied Physics*, vol. 74, no. 9, p. R83, 1993.
5. W. R. Levick, "Another tungsten microelectrode", *Medical & Biological Engineering*, vol. 10, no. 4, pp. 510–515, 1972.
6. R. Hobara et al, "Dynamic electrochemical-etching technique for tungsten tips suitable for multi-tip scanning tunneling microscopes", *E-J. Surf. Sci. Nanotechnol.*, vol. 5, no 0, p. 94 98, 2007.
7. B.-F et al, "The art of electrochemical etching for preparing tungsten probes with controllable tip profile and characteristic parameters", *Rev. Sci. Instrum.*, vol. 82, no 1, p. 013707, janv. 2011.
8. <https://www.goodfellow.com>

# Elaboration of high-entropy coating by cold spray followed by laser melting

A. Sova<sup>1</sup>, M. Doubenskaia<sup>1</sup>, E. Trofimov<sup>2</sup>, M. Samodurova<sup>2</sup>, V. Ulianitsky<sup>3</sup>

<sup>1</sup>University of Lyon, National Engineering School of Saint-Etienne (ENISE), LTDS Laboratory  
58 rue Jean Parot, Saint-Etienne, France, alexey.sova@enise.fr, maria.doubenskaia@enise.fr

<sup>2</sup>South Ural State University  
76 Lenin Ave, Chelyabinsk, 454080, Russian Federation, trofimovea@susu.ru,  
samoduriiovamn@susu.ru

<sup>3</sup>Laboratory of Synthesis of Composite Materials, Institute of Hydrodynamics M.A. Lavrent'ev SB  
RAS  
15 Lavrent'ev Av., Novosibirsk, Russian Federation, ulianv@mail.ru

## Abstract

The feasibility study of elaboration of high-entropy alloy coating by hybrid approach including cold spray and laser remelting was performed. At the first stage the 2-mm thick composite precursor coating was deposited on aluminum substrate by cold spray using mixture of four metal powders. At the second stage the laser melting of 500  $\mu\text{m}$  layer at the top surface of composite coating was successfully performed. The microstructure analysis revealed good element mixing in the melting pool during laser melting. EDS and phase analysis showed that the remelting zone consist of  $\text{Al}_{0.1}\text{CuCr}_{0.5}\text{FeNi}_{0.5}\text{Mo}_{0.2}$  composition. The resulting composition differed from the targeted one due to different deposition efficiencies of the powders during cold spraying. The developed approach could be applied for elaboration of other high-entropy alloy coatings.

**Keywords:** high-entropy alloy, coatings, composite, cold spray, laser melting

## 1. Introduction

High-entropy metal alloys (HEA) are considered as advanced materials with significant application potential in different domains of industry [1, 2]. Recent studies revealed unique mechanical properties of HEA coatings deposited on metal substrates [2]. In general, the HEA coatings are elaborated by laser cladding [3], thermal spray [4-6] or cold spray [7, 8] techniques using pre-alloyed HEA powders. The main drawback of these approaches is the low commercial availability of HEA powders. Alternative way of deposition of HEA coatings is *in situ* synthesis of high-entropy phases during laser cladding of powder mixtures of pure metals or low-entropy alloys [9]. In this case, all the components of the powder blend melt and mix in the molten pool. Formation of HEA phase occurs during molten pool solidification [9]. However, this approach is not applicable for formation of thick HEA coatings on aluminum parts due to low melting temperature.

In this work the feasibility study of the two-stage hybrid approach of HEA coating deposition on aluminum substrate was proposed. At the first stage of this process, the precursor composite coatings containing the mixture of several low-entropy powders is elaborated by cold spray on aluminum alloy substrate. At the second stage, the formation of HEA phases in the coating is promoted by laser remelting of near-surface zone of the coating. The approach is illustrated in Figure 1. The targeted composition of HEA was selected only for research purpose in order to verify the feasibility of proposed hybrid approach.

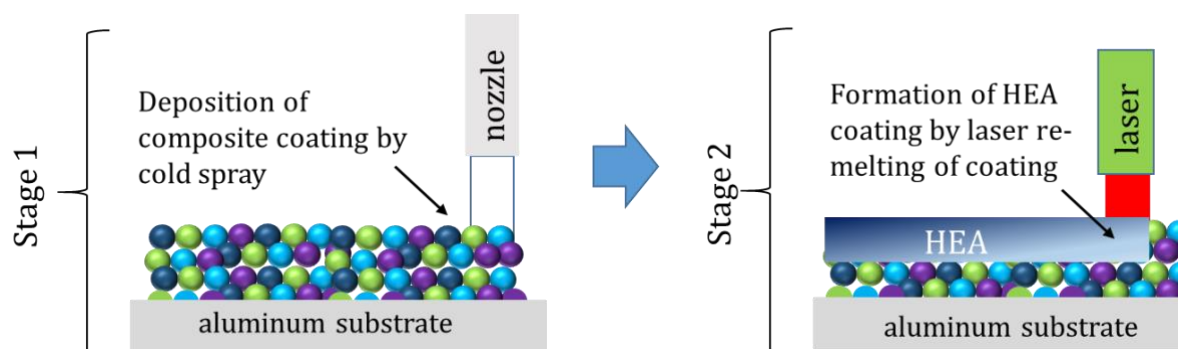


Figure 1: Schematics of two-stage hybrid approach of high-entropy alloy coating deposition

## 2. Materials and methods

At the first stage the precursor metal composite coating was deposited on grinded aluminum substrate by cold spray. The pure copper, pure aluminum, 316L and Tribaloy T700 powders were considered as the primary material containing Al, Cu, Fe, Ni, Cr and Mo necessary for synthesis of targeted high-entropy phase. At the second stage, the top surface of the coating was subjected to laser melting. During laser treatment full melting of particles of all coating components was expected. The parameters of the cold spray deposition as well as the laser melting are presented in Table 1.

Table 1: Parameters used for cold spray coating deposition and following laser melting

cold spray deposition					
Equipment	Gas type	Gas pressure	Gas temperature	Spray distance	Nozzle speed
Kinetiks 4000 / nozzle OUT-1	Nitrogen	35 bars	650 °C	30 mm	50 mm/s
laser melting					
Equipment	Power	Spot diameter	Speed	Scan strategy	Line superposition
Precitec / Laserline LDM 980 nm	1 kw	2 mm	13 mm/s	Parallel lines	1 mm

The morphology of the powders, the microstructure and EDS analysis of the coatings was performed by scanning electron microscope TESCAN VEGA. XRD analysis was performed using Bruker D8 Advance diffractometer (Bruker AXS, Germany). Porosity of the coatings was evaluated by image analysis.

## 3. Results and discussion

In order to obtain the targeted element composition, the cold spraying of four-component mixture with mass composition 316L (41%) + Tribaloy 700 (47%) + Cu (10.5%)+Al (1.5%) was performed at the first stage. The composite coating was successfully deposited. The coating microstructure is presented in Figure 2a. The particles of copper and aluminum exhibited sever deformation at impact, whereas hard particles of T700 alloy preserved its initial spherical shape. Particles of all powders are uniformly distributed in the coating. It is important to note, the uniform particle distribution is the key factor for formation of high-entropy phases during laser melting. The EDX analysis showed that the coating element composition differed from the targeted one (Table 2). The composition mismatch is explained by different deposition efficiency of the powder mixture components that is typically observed in case of cold spray of the powder mixtures having significantly different mechanical properties [10]. Thus, the deposition efficiency of T700 powder was the lowest one. The maximum deposition efficiency was observed for aluminum and copper powders. As a results, the content of nickel and molybdenum in the coating is approximately two times smaller than for the targeted composition. Besides low deformation of T700 particles, the porosity of the coating was below to 1% due to significant deformation at impact

of other mixture components. The laser melting of composite coating was successfully performed. The SEM images of the coating after laser remelting at different magnifications are presented in Figure 2b.

Table 2: Comparison of initial mixture composition with the coating composition before and after laser melting

	Initial blend composition, at. %	Precursor coating composition at. %	Composition after remelting at. %
Ni	28.35	14.4	14.6
Fe	29.8	30.2	30.3
Mo	10	5.5	5.5
Cr	15.8	12.5	12.6
Cu	9.7	31.2	31.3
Al	3.2	3.5	3.1
Si	2.5	2.1	2
Other	0.65	0.6	0.6

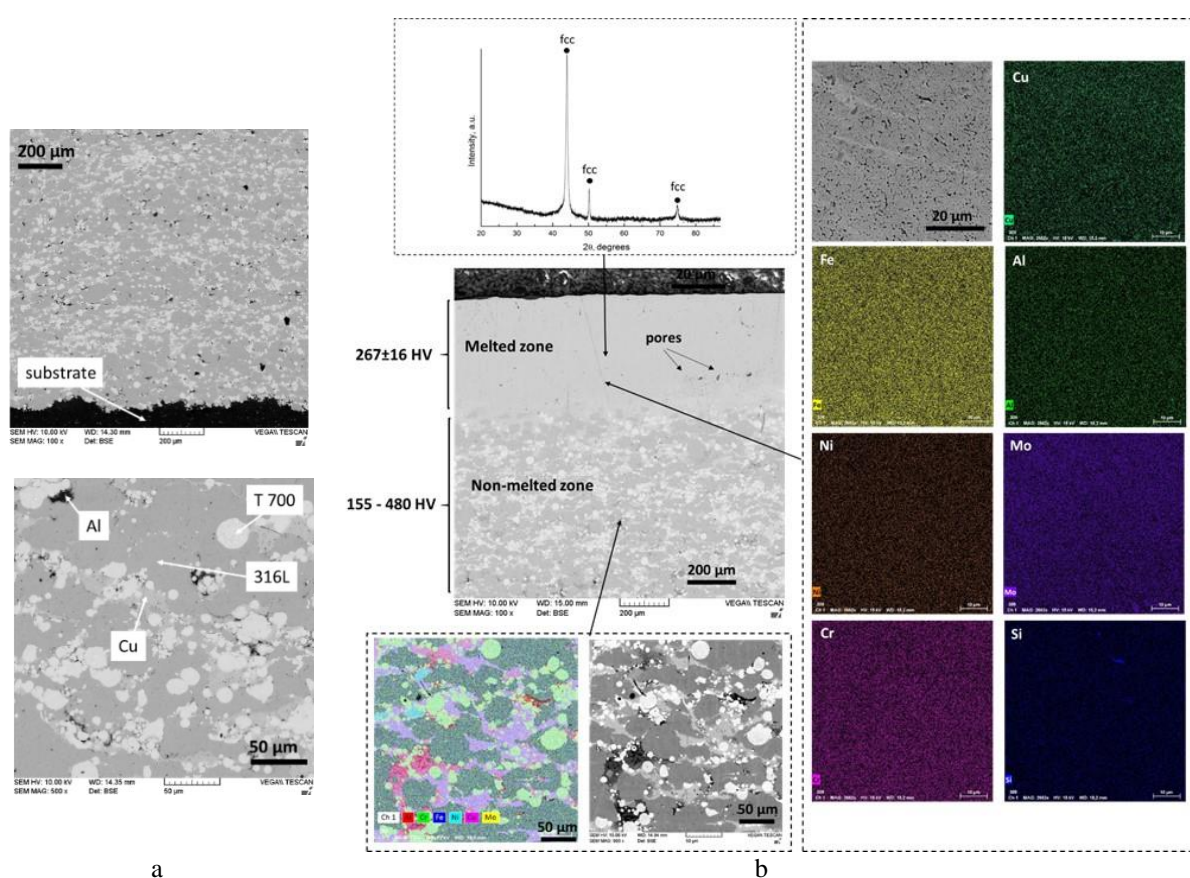


Figure 2: Microstructure of as-sprayed (a) and remelted (b) coating

The selected laser parameters allowed complete melting of the top zone of cold spray composite coating. The depth of molten pool was near ~500  $\mu\text{m}$ . No cracks or large-scale defects were found in the interface between melted zone of the coating and non-melted one. Some spherical gas pores were nevertheless found in the melted zone. The overall porosity of the melted layer was less than 1%. All particles formed initial structure of as-sprayed coating were melted during laser treatment. EDS analysis performed at non-melted and melted zone showed that the elements are uniformly distributed in the coating after melting (Figure 3b). The element composition of melted zone showed slight decrease of aluminum content in comparison with initial coating that indicates on partial evaporation of aluminum during laser treatment. One can conclude that the element diffusion in molten pool during laser treatment allowed efficient material mixing in liquid state. As a consequence, no zones rich in some particular element were found in melted zone. The XRD patterns revealed the melted zone had face centered cubic (fcc) structure that indicates on formation of uniform solid solution that is typical for high-entropy alloy with

this chemical composition. The microhardness measurements were performed at both non-melted and melted zones. The hardness of melted zone was stable and equal to  $267 \pm 16 \text{ HV}_{0.3}$  whereas the hardness of non-melted zone varied from 155 to 480 HV depending on the indentation point. Large variation of hardness in non-melted zone is explained by significant hardness difference between the T700, 316L, Al and Cu particles.

#### **4. Conclusions**

The possibility of obtaining of high entropy alloy coatings by hybrid approach combining cold spray and laser melting was investigated. The cold spray deposition of particles of the metals occurred in solid state with different deposition efficiencies. As a result, the coating composition differed from the targeted one. The deposited layers had a composite structure consisting of deformed particles of all mixture components with residual porosity below 1%. Followed laser melting allowed formation of uniform layer with visible gradient between melted and non-melted zones. Applied laser melting parameters allowed formation of uniform structure due to efficient material melting and mixing on molten pool. The final composition of remelted layer was  $\text{Al}_{0.1}\text{CuCr}_{0.5}\text{FeNi}_{0.5}\text{Mo}_{0.2}$

Developed approach could be applied for elaboration of high-entropy alloy coatings with other compositions. However, the main challenge in this approach is proper fabrication of cold spray precursor coating with targeted element composition. To reach this goal, the pure powders of metals could be applied instead of alloy powders used in this study.

#### **5. Acknowledgements**

This work was supported by the Russian Science Foundation (project No. 20-19-00304).

#### **6. References**

1. J.M. Torralba et al. “High-entropy alloys fabricated via powder metallurgy. A critical review”, *Powder Metall.*, vol. 62, no. 2, pp. 84-114, 2019
2. A. Ostovari Moghaddam et al., “Additive manufacturing of high entropy alloys: a practical review” *J. Mater. Sci. Technol.*, vol. 77, pp. 131-162, 2021
3. T.M. Yue et al., “Solidification behaviour in laser cladding of AlCoCrCuFeNi high-entropy alloy on magnesium substrates”, *Journal of Alloys and Compounds*, vol. 587, pp. 588-593, 2014
4. W.-B. Liao et al., “Microstructures and mechanical properties of CoCrFeNiMn high-entropy alloy coatings by detonation spraying”, *Intermetallics*, vol. 132, art.no.107138, 2021
5. A. Ang, et al., “Plasma-sprayed high entropy alloys: Microstructure and properties of AlCoCrFeNi and MnCoCrFeNi”. *Metall. Mater. Trans. A* , vol. 46, pp. 791–800, 2015
6. W. Hsu, et al., “On the study of thermal-sprayed  $\text{Ni}_{0.2}\text{Co}_{0.6}\text{Fe}_{0.2}\text{CrSi}_{0.2}\text{AlTi}_{0.2}$  HEA overlay coating”, *Surf. Coat. Technol.*, vol. 316, pp. 71–74, 2017
7. J. Lehtonen et al., “Cold Gas Spraying of a High-Entropy CrFeNiMn Equiatomic Alloy”, *Coatings*, vol. 10 no 1, 2020
8. S. Yin et al, “Deposition of FeCoNiCrMn high entropy alloy (HEA) coating via cold spraying”, *Journal of Materials Science & Technology*, vol. 35, no 6, pp. 1003-1007, 2019,
9. A.Ostovari Moghaddam et al., “A novel intermediate temperature self-lubricating CoCrCu1-xFeNix high entropy alloy fabricated by direct laser cladding”, *Tribology International*, vol.156, art. no. 106857, 2021,
10. L. He, M. Hassani, “A Review of the Mechanical and Tribological Behavior of Cold Spray Metal Matrix Composites”, *Journal of Thermal Spray Technology*, vol. 29, no. 7, pp. 1565-1608, 2020

# **Methodology for Designing the Parameters of Technological Nitriding Regime with Respect to the Relative Wear Resistance of Tool Steels for hot Working**

**Nikolay Tontchev<sup>1</sup>, Emil Yankov<sup>2</sup>, Angel Zumbilev<sup>3</sup>**

<sup>1</sup> University of Transport, 158 Geo Milev Str, 1574, Sofia, Bulgaria, tontchev@vtu.bg

<sup>2</sup> University of Ruse „Angel Kanchev“, 8 Studentska Str., 7017, Ruse, Bulgaria, eyankov@uni-ruse.bg

<sup>3</sup> Technical University – Sofia, Plovdiv branch, 26 Tsanko Dyustabanov Str., Plovdiv, Bulgaria, zumbilev@mail.bg

## **Abstract**

This study aims to create a methodology for decision making in the process of designing the regime of the technological process of nitriding. The methodology is applied for relative degree of wear  $K_v$  for grade tool steels for hot working BH10, BH11 and BH21 and thus the stages of its implementation are demonstrated. They are used based on procedures such as Design of Experiment, optimization with one and many criteria. With the help of the numerical methodology the tendency in the change is determined for establishing technological regimes and modeling properties of wear, which are finally clarified by nitride zone forming the layer. Since the analyzed steels are of the same class, the study establishes the general processing regime which leads to the desired relative wear resistance. The research was accompanied by the receipt of specific values for the relative degree of wear  $K_v$  and their corresponding regimes for the three tested steels. Through the stages of the applied methodology, a general range has been determined for the whole class in which the steels have high wear resistance.

**Keywords:** Aon nitriding, Plasma nitriding layers, Modeling properties of wear, Grade tool steels for hot working

## **1. Introduction**

The tribological characteristics of systems, whether nano, micro or macro-scale, depend on many external parameters. The most important among them are the temperature and the operating conditions, the contact pressure and the relative speed of the contact parts. These basic parameters affect the operational surface properties of structural and tool steels. In [1] the modern tendencies in the research of the tribological characteristics of the systems are indicated, as the emphasis is placed in the industrial applications of the tribology. The surface integrity during processing is summarized in [2], which describes the basic achievements in the study of contact strength after chemical heat treatment. Tribological issues, and those related to wear resistance, need to be identified before the process of designing treatment regimes when it comes to thermal or chemical treatment. In this case, the concept of tribology will be most useful in practice. This idea is shared in [3], which brings together original and innovative research on applications in tribology, contributed by a group of selected researchers describing the best of their work. Similar studies are described in the monograph [4], where the relationship between the goal parameters and the technological factors of the modes for processing are defined. The brief overview of this research can determine the characteristics of the chosen topic, which is associated with complexity and nonlinearity, in terms of composition of the rising most often absorbent limits, as well as the different properties of materials in depth of the examined surfaces. The considered significant change individually or as a complex affects the wear resistance, corrosion resistance, resistance to high values of the fatigue cycle, which are the components to new surface conditions [5]. These new surface conditions are formed by a desired set of properties, which is determined by solving multicriteria problems [6, 7]. The latter guarantee the identified benefits to the study, most often expressed in increased longevity (extended life) of contact articles [8, 9]. All this is associated with the resource for production, characterization, and applications in the field of hard coatings and wear-resistant surfaces. In [10] a full explanation of the deposition technology of traditional vacuum-based thin film coatings, such as evaporation, chemical vapor

deposition, is discussed. This review would be more purposeful if an analytical or numerical methodology could be formulated to establish the influence of different regimes equally influencing a whole class of steels. In this way the private influence of one or another alloying element, such as its concentration and combination with the other elements, will be ignored.

## 2. Purpose of the Research

The aim of the research is to apply a methodology for the analysis of wear resistance of BH10 BH11 and BH21 steel, with the intention completely to clarify the role of the technological modes on its influence. However, since the research is based entirely on an experimental-statistical basis, the results obtained will be compared and explained by the accumulated experience of the authors and with the phase composition. The methodology must be able to determine an appropriate mode satisfactory for the whole class of tested steels. The defined general technological modes and the substantiation made on them will help to fully clarify the further research. This will overcome a multifactorial, nonlinear problem described by dependencies reflected in [11], which is difficult to interpret and compare.

## 3. Stages, Operational Sequence of Work and Results From the Application of the Methodology

The design object is selected. It is necessarily related to a technological process, the parameters of which vary in range. The input and output parameters of the research are defined for the object of the study. The object of research with which the methodology is tested in this case is determined by three types of tool steels. Steels BH10 and BH11 have an increased heat resistance and toughness, and steel BH21 is with a high heat resistance. The chemical composition and some important characteristics of these steels are listed in Table 1.

Table 1: Chemical composition of steel from the class, [%].

Steel	C	Si	Mn	Cr	Mo	W	V	Ni	Cu	S
BH11	0.38	0.91	0.22	4.5	1.20	–	0.47	0.14	0.11	0.006
BH10	0.28	0.45	0.20	3.24	2.74	–	0.55	0.13	0.12	0.01
BH21	0.3	0.18	0.26	2.7	–	8.01	0.29	–	–	0.015

### 3.1. The Parameters and the Interval of their Change are Determined

Based on bibliography data and preliminary experiments, the following input (control) factors [4] must be determined: the nitriding temperature, the pressure, the duration of the process, and the temperature of tempering. Based on the influence of various factors on the ion nitriding and the objectives pursued, the following parameter were selected for optimization relative degree of wear  $K_v$  for grade tool steels for hot working BH10, BH11 and BH21. Table 3 shows the main levels of variation of the input parameters with which the experiment is planned.

### 3.2. An Experiment is Planned with the set Levels of Change, in Which for Each Changing Combination of the Input Data, an Average Value of the Controlled Value Corresponds – the Relative Wear Resistance $K_v$

To determine the nitriding regimes mathematical and statistical methods of the planned experiment have been used.

Table 2: Characteristics of the steels.

Factors	$t_{nit}$ [°C]	P [Pa]	$\tau$ [h]	$t_{tem}$ [°C]
Levels X	$X_1$	$X_2$	$X_3$	$X_4$
Zero level (0)	530	300	7	650
Interval of variation	20	150	3	50
Upper level (+I)	550	450	10	700
Lower level (-I)	510	150	4	600

A characteristic of this approach is that a compulsory change of input factors is performed within certain limits, determined by Table 2. A minimal number of trials and simultaneous adjusting of all factors is used. Selected in this way, the factors and intervals are also used to design experiments based on a plan of the various combinations of processing-mode parameters which the experiments were conducted with. To reduce the errors, it is recommended that every attempt must be repeated and the combinations of zero-level factors five times. All samples were ion nitrided in an installation of type ION-20 [4]. The impregnation gas during nitriding in glow discharge was gaseous ammonia. After nitriding, the samples were cooled in air. The experimental conditions and the test scheme for relative wear resistance are given in [4].

After conducting the experiment, using a standard statistical procedure described in [12] adequate models are derived. After checking the adequacy of the models, the specific design results are determined.

Adequate regression models have been derived for the relative wear resistance –  $K_V$  based on 30 different [4] combinations of these parameters using an experimental design and a statistical method described via the following equations:

$$K_V = 0.4020 - 0.0828 \times X_1 + 0.0033 \times X_2 - 0.0523 \times X_3 - 0.0008 \times X_4 + 0.0037 \times X_1^2 + 0.0106 \times X_1 \times X_2 + 0.0244 \times X_1 \times X_3 - 0.0006 \times X_1 \times X_4 + 0.0087 \times X_2^2 - 0.0469 \times X_2 \times X_3 + 0.0031 \times X_2 \times X_4 + 0.0237 \times X_3^2 + 0.0093 \times X_3 \times X_4 + 0.0512 \times X_4^2 \quad (1)$$

$$K_V = 0.3898 - 0.0786 \times X_1 - 0.0099 \times X_2 - 0.0494 \times X_3 + 0.0151 \times X_4 + 0.0307 \times X_1^2 + 0.0131 \times X_1 \times X_2 + 0.0044 \times X_1 \times X_3 + 0.0157 \times X_1 \times X_4 + 0.0257 \times X_2^2 - 0.0494 \times X_2 \times X_3 + 0.0243 \times X_2 \times X_4 + 0.0107 \times X_3^2 - 0.0218 \times X_3 \times X_4 + 0.0457 \times X_4^2 \quad (2)$$

$$K_V = 0.3804 - 0.0804 \times X_1 - 0.0076 \times X_2 - 0.0504 \times X_3 + 0.0300 \times X_4 + 0.0156 \times X_1^2 + 0.0050 \times X_1 \times X_2 - 0.0025 \times X_1 \times X_3 + 0.0037 \times X_1 \times X_4 + 0.385 \times X_2^2 - 0.054 \times X_2 \times X_4 - 0.029 \times X_3^2 - 0.037 \times X_3 \times X_4 + 0.059 \times X_4^2 \quad (3)$$

Equation (1) applies to BH11 steel, (2) to BH10 steel and (3) to BH21 steel.

### 3.3. After the Modeling Process, Single-Criteria and Multi-Criteria Optimization is Performed, Which Generalizes the Technological Design Solutions

This is an essential prerequisite for solving optimization problems, as it reflects the principled nature of the search processes for the best result, regardless of the nature of the object of optimization and the goal. A full description of the idea at this point, including with appropriate examples, is considered in [11]. Most optimization problems are characterized by a variable number of optimization variables. The algorithm proposed in [11] is classical because it turned out that the controlled factors have a constant step of change. The application of other currently evolving algorithms is certainly able to provide much more accurate solutions, but in fact at the stage of implementation they cannot be realized by the technique provided by the respective mode. After defining equations (1), (2) and (3) in Section 3 and determining their identifiers using the author's approach, the problem finds its

solution. Since the maximal wear resistance occurs at a minimal value of the wear coefficient  $K_v$ , then the task of the research is transformed into a search for a treatment mode that simultaneously provides a minimal value of  $K_v$  and the three regression models (1), (2) and (3). At the beginning, for each of the models (1), (2) and (3) an optimization is performed for the relative wear coefficient  $K_v$  in which the minimal and maximal values of this goal value are determined. Despite the fact that the parameter is the same, due to the different composition of the steel, a certain inconsistency of the criteria was established. This is typical of most engineering applications. The result of the single-criteria optimizations is presented in Table 3.

In this case, the designer encounters objective difficulties in formulating a general mode for the considered technological process. In this case, the constraints are imposed on the design variables and performance criteria using models (1), (2) and (3) according to the methodology described in [11].

In this case, the designer encounters objective difficulties in formulating a general mode for the considered technological process. In this case, the constraints are imposed on the design variables and performance criteria using models (1), (2) and (3) according to the methodology described in [11].

Table 3: Results of the performed single-criteria optimization for the studied steels.

Parameter	Steel	Value	Processing mode			
			$t_{nit}$ [°C]	$P_{NH_3}$ [Pa]	$\tau_{nit}$ [h]	$t_{tem}$ [°C]
Regimes of Min values of $K_v$	BH11	0.2944	550	450	10	600-620
	BH10	0.2549	550	450	10	600
	BH21	0.237	550	300	10	600-620
Regimes of Max values of $K_v$	BH11	0.6984	510	450	4	670-700
	BH10	0.7515	510	450	4	670-700
	BH21	0.97	510	150	4	670

However, these constraints are precisely the identifiers for the minimum, maximum, or interval of values in each range imposed on regression models (1), (2) and (3). They significantly determine the set/complex of feasible solutions that meet all the necessary requirements for the design task. Without constructing this set / complex of additional requirements to optimize the solution, the solution of the defined problem often turns out to be useless.

The choice of a particular method is determined by requirements and the nature of the object and by the correct definition of the optimization problem. The criterion for optimality for technological objects is expressed by three objective functions.

Principally the optimization is carried out under direct experimentation with the object of the scheme: control action – the result – a new control action. In principle, the optimization is performed by direct experimentation with the object of the scheme: control action – result – new control action. In practice, however, the optimization research is carried out with the object or the system represented by a mathematical model.

Table 4: Results of the performed single-criteria optimization for the studied steels.

Parameter	Steel	Value of $K_v$	Normalized percentage	Processing mode			
				$t_{nit}$ [°C]	$P_{NH_3}$ [Pa]	$\tau_{nit}$ [h]	$t_{tem}$ [°C]
Regime of Min values of $K_v$	BH11	0.3187	6.07 %	550	300	10	600
	BH10	0.263	5.07 %				
	BH21	0.237	0.00 %				

The results listed in Table 4 concern the factors determined by the regression models in this way. The values of the target parameters in Table 4 can be normalized respectively to the smallest and largest values of the considered

feature of the class normalized to the smallest and largest values of the considered characteristic of the class, respectively.

With the defined in Table. 4 mode a real practical experiment was performed, and the error of the predicted and modeled values is within the allowable statistical error of 0.05%.

#### **4. Conclusion**

Based on the proposed approach to the problem of selection of technological solutions, considering the provision of information, procedures have been developed to search for the respective regime, supplementing the archives of technological solutions. The research has the claim to offer an adapted optimization approach that the same can be applied to a set of materials from a similar class, with the help of which to determine generalized regimes common to the whole class of materials. The approach is applicable at the stage of designing technological modes and it can be applied to any studied quality indicator of interest to the user.

#### **Acknowledgements**

The research and the participation in this scientific conference were implemented with the support of the: Research and Development at the Technical University of Sofia for the financial support; Research Fund at University of Transport „Todor Kableshev“ by contract project № 90-05-20 for “Contribution of VTU in the analysis, modeling and optimization of simulation and experimental databases”; Research Fund at University of Ruse „Angel Kanchev“ by contract project FMME 2020-01 for „Research of laser and layer-by-layer technologies for obtaining prototype models“.

#### **References**

1. Katiyar J.K., Ramkumar P., “Rao T.V.V.L.N” in *Tribology in Materials and Applications*, Davim J.P. (Eds.), Springer, Materials Forming, Machining and Tribology, 2020. – 306 p.
2. Paulo D.J., “Surface Integrity in Machining”, Springer, 2010, 222 p.
3. Darji P.H. (Ed.), “Advances in Tribology” in *ExLi4EvA*, 2016, 271 p.
4. Zumbilev A.P., Zumbilev I.A., “Ionic nitriding and carbonitriding of steels” in Bulgarian, 2020, 325p.
5. Zumbilev I. “Carbonitriding austenite steel in glow discharge plasma” in *Journal “Annals of the Faculty of Engineering Hunedoara”*, vol. 14, Fascicule 1 (ISSN1584-2665), Romania, 2016, pp.203 – 206.
6. Abdelkhalik O., “Engineering Systems Optimization” in *Boca Raton: CRC Press*, 2021, 230 p.
7. Statnikov R.B., Matusov J.B., “Multicriteria Optimization and Engineering” in Springer, 1995, 250.
8. Zumbilev I., „About the influence of ion carbonitriding on the chemical composition of the carbonitride zone“ in *Journal of Food and Packaging Science, Technique and Technologies*, vol 8, National Academy of Packaging – Bulgaria, 2016, pp.10-13.
9. Zumbilev I., “About wear resistance of nitrided and carbonitrided layers” in *Journal “Annals of the Faculty of Engineering Hunedoara”*, vol. 8, Fascicle 1, Romania, 2015, pp. 53-56.
10. Bunshah Rointan F. (ed.), “Handbook of Hard Coatings” in *Deposition Technologies, Properties and Applications*, Noyes publications, 2001, 560 p.
11. N. Tontchev, “Effective solutions, and technological variants” in *Materials science*, Lambert, Academic Publishing, 2014. 173 p
12. Vuchkov, I., L. Boyadjieva, “Quality Improvement with Design of Experiments”, A Response Surface Approach, 2001, 364 p.